Nanoscale

ROYAL SOCIETY OF CHEMISTRY

PAPER

View Article Online
View Journal

Cite this: DOI: 10.1039/d6nr00321d

2D black phosphorus as a phosphide source for the formation of mixed cobalt phosphide clusters active in photocatalytic hydrogen evolution

Giacomo Provinciali,[a] Manuel Serrano-Ruiz, [a] Jonathan Filippi,[a] Beatrice Muzzi,[a] Martina Banchelli, [b] Carlo Calcatelli, [c,d] Alberto Verdini, [d] Stefano Caporali,[e] Francesco D'Acapito, [f] Maurizio Peruzzini[a] and Maria Caporali *[a]

Received 23rd January 2026,
Accepted 16th March 2026

DOI: 10.1039/d6nr00321d

rsc.li/nanoscale

The use of solar energy to produce valuable feedstocks and energy vectors, such as hydrogen, is a fascinating research field of utmost practical importance. Herein, we report a facile strategy to functionalize 2D black phosphorus nanosheets (BPNS) with mixed cobalt phosphide clusters of different stoichiometry, Co_2P and CoP, with sub-nanometric sizes. The in-depth study at the atomic level by X-ray absorption spectroscopy and electron microscopy confirmed the nature and structure of the phosphides and revealed that Co_2P/CoP functionalization effectively hindered the spontaneous degradation of BP under ambient conditions. Under simulated solar-light irradiation, the hydrogen evolution rate of BP@Co_xP integrated with TiO_2 reached 5.3 mmol g^{-1} h^{-1}, almost 30-fold higher than that of TiO_2. Electrochemical and photoluminescence investigations elucidated the electronic properties of the photocatalyst, showing that the mixed Co_xP phases led to increased charge density across the heterostructure, a lower conduction band energy, which infers more reducing power, and the generation of multiple interfaces, which increase charge transfer and reduce electron–hole recombination.

Introduction

The increasing need for global sustainable development through the supply of clean energy has pushed researchers to look for alternative ways to drive chemical processes, taking advantage of renewable energies and avoiding toxic reagents and critical raw materials.[1] In recent years, there has been a rising interest in the use of solar energy to trigger different chemical reactions, such as the hydrogen evolution reaction (HER),[2] the oxygen evolution reaction (OER),[3] CO_2 reduction,[4] N_2 fixation and environmental remediation.[5] A variety of inorganic semiconductors have been employed as photocatalysts, and, from these, 2D black phosphorus (BP) has emerged. BP is a direct semiconductor endowed with a narrow band gap (0.3 eV in the bulk and 2.0 eV in the monolayer) that enables absorption of visible and near-infrared light, thus covering a considerable part of the solar light spectrum. Additionally, BP is endowed with an intrinsic chemical reactivity[6] because its lone pairs, localized on each P atom, enable it to participate in diverse reactions with molecules and materials through either covalent or non-covalent interactions.[6] Extensive work has been done to achieve the functionalization of BPNS with transition metal oxides and sulfides[7] and to elucidate the activity in various photocatalytic processes, such as the HER. Nanohybrids of BP with cobalt have shown good performance in the HER, and different procedures have been developed for their synthesis. For instance, A. Ozawa *et al.* synthesized BPNS by a solvothermal reaction from RP in ethylenediamine before loading Co nanoparticles (NPs) (1.1 wt%) on BP by photodeposition, reaching an enhanced HER rate of 480 μmol g^{-1} h^{-1}.[8] X. Ren *et al.* performed the calcination of solid BPNS and $CoCl_2$ at 300 °C for 2 h under an Ar atmosphere,[9] and the resulting nanohybrid was described as featuring single cobalt atoms anchored on BPNS.

Our aim was to focus on BP functionalization with cobalt phosphides, as it is known that the latter may significantly lower the reduction potential of water[10] and have high conduc-

---

[a] *Institute of Chemistry of OrganoMetallic Compounds, National Council for Research, CNR-ICCOM, Via Madonna del Piano 10, I-50019 Sesto Fiorentino, Italy. E-mail: maria.caporali@iccom.cnr.it*

[b] *Institute of Applied Physics "Nello Carrara", National Council for Research, CNR-IFAC, Via Madonna del Piano 10, I-50019 Sesto Fiorentino, Italy*

[c] *Department of Physics and Geology, University of Perugia, Via A. Pascoli, 06123 Perugia, Italy*

[d] *CNR-IOM, Perugia Unit, c/o Department of Physics and Geology, University of Perugia, Via A. Pascoli, 06123 Perugia, Italy*

[e] *Department of Industrial Engineering, University of Florence, Via di S. Marta 3, 50139 Firenze, Italy*

[f] *CNR IOM-OGG, c/o European Synchrotron Radiation Facility, 71 Avenue des Martyrs, CS 40220, 38043 Grenoble, Cedex 9, France*

tivity, which is highly beneficial for the HER process. For these reasons, cobalt phosphides have demonstrated greater efficiency than platinum in the HER process.[8,11] We also envisaged an alternative way of functionalizing BP with cobalt by conducting a mild solvothermal process that avoids drastic thermal treatment, which may cause extensive degradation of BPNS, and using the P atoms as a *phosphide source* to generate Co_xP species *in situ*. Unexpectedly, under our selected reaction conditions, a mild phosphating process took place in which the BPNS act as both a substrate for growth and a reagent, affording mixed Co_2P and CoP clusters homogeneously dispersed on the surface of the BPNS. Previous studies have shown the decoration of BP with nanostructured cobalt phosphide,[10,12,13] or with single cobalt atoms;[9] in this work, the formed Co–P species have sizes ranging from molecular clusters to nanocrystals. Given that the size is connected to quantum confinement effects and absorption properties, this opens the possibility of changing the electronic properties and consequently the photocatalytic behavior. The binary composites BP@Co_xP were self-assembled with TiO_2, and their activity in the solar-driven production of H_2 was evaluated. As a result, a greatly improved HER rate was observed that was almost 30 times higher than that of pristine TiO_2, even when working with a very low Co content (<1%). In-depth studies at the atomic level by XAS and electron microscopy confirmed the nature and structure of the composite and revealed that Co_xP functionalization contributed to effectively preventing the ambient degradation of BP.

Experimental section

Materials

Red phosphorus (99.99% purity), TiO_2 (Degussa P25), Co$(CH_3COO)_2\cdot 4H_2O$, $CoCl_2(PPh_3)_2$, and $CoCl(PPh_3)_3$ were purchased from Merck. CoP was prepared as previously described.[14]

Exfoliation of bulk black phosphorus

First, black phosphorus crystals were synthesized from red phosphorus according to a published procedure.[15] Afterwards, few-layer black phosphorus nanosheets were obtained by liquid-phase exfoliation of black phosphorus crystals in dimethylsulfoxide using an ultrasonication bath, as previously described by some of us.[16]

Synthesis of BP@Co_xP binary composites

The procedure is a slight modification of the published protocol.[17] First, BPNS (3.0 mg, 0.096 mmol) were suspended by ultrasonication in 3 mL of dry DMF, and, separately, Co$(CH_3COO)_2\cdot 4H_2O$ (1.3 mg, 0.006 mmol) was solubilized in 12 mL of dry DMF. To the solution of cobalt acetate, BPNS suspension was added under stirring at 800 rpm. The mixture was transferred to a Teflon-lined stainless-steel autoclave (volume of 30 mL) that was sealed tightly under N_2 to prevent exposure to ambient humidity and oxygen. The sealed autoclave was transferred to an oven, and the solvothermal process was carried out at 180 °C for 4 hours. After the autoclave was cooled to room temperature, the sediment was collected by centrifugation at 8000 rpm. Three washing/centrifugation cycles were carried out using degassed ethanol, then the solid BP@Co_xP 10 wt% was dried under vacuum overnight. For comparison, a series of binary composites BP@Co_xP were obtained, where x represents the weight percentages of Co in the various composites, x = 10, 20 and 30 wt%, respectively.

Synthesis of TiO_2/BP composite

This material was prepared by following a procedure reported by some of us.[14] Four binary composites were synthesized with a BP content of 1.0, 2.0, and 3.0 wt%.

Synthesis of TiO_2/BP@Co_xP ternary composites

TiO_2 (22.3 mg, 0.279 mmol) and 0.25 mg of the prepared BP@Co_xP 10 wt% were dispersed in 15 mL of N_2-degassed 2-propanol. The dispersion was ultrasonicated (170 W, 35 kHz) for 3 hours, keeping the temperature of the sonication bath fixed at T = 17.5 °C. Afterwards, the gray powder of TiO_2/BP@Co_xP was isolated by centrifugation. Two washing/centrifugation cycles were carried out using degassed methanol, then the solid was dried under vacuum overnight. A series of TiO_2/BP(y)@Co_x(z)P composites were obtained using different starting binary composites, where y and z represent the weight percentages of BP and Co in the various composites, y = 1.0%, 2.0%, and 3.0% and z = 0.1%, 0.2%, 0.3%, 0.4%, 0.6%, 0.8%, and 0.9%.

Characterization

X-ray diffraction (XRD). Data were collected on the powder samples with an X'Pert PRO diffractometer, operating in Bragg–Brentano parafocusing geometry with a Cu target and Kα radiation (λ = 1.5418) at 40 kV beam voltage and 40 mA current. The data were collected in the 5°–90° 2θ range, with steps of 0.01° and a counting time of 130 s.

Transmission electron microscopy (TEM). TEM images were acquired using a Thermo Fisher Talos F200X G2 at an accelerating voltage of 200 kV and a camera resolution of 4096 × 4096 pixels. The energy-dispersive X-ray spectroscopy (EDS)-scanning electron microscopy (STEM) maps were recorded with a Super X spectrometer equipped with four 30 mm^2 silicon drift detectors with a collection angle of 0.7 sr.

X-ray photoelectron spectroscopy (XPS). XPS measurements were performed at the Chemistry Department, University of Florence (Italy) in an ultra-high vacuum (10^{-9} mbar) system equipped with a VSW HAC 5000 hemispherical electron energy analyzer and a non-monochromatized Mg-Kα X-ray source (1253.6 eV). The source power used was 100 W (10 kV × 10 mA), and the spectra were acquired in the constant-pass-energy mode at E_{pas} = 44 eV. The overall energy resolution was 1.2 eV as a full-width at half-maximum (FWHM) for the Ag $3d_{5/2}$ line of a pure silver reference. The recorded spectra were fitted using XPS Peak 4.1 software employing Gauss–Lorentz curves after subtraction of a Shirley-type background. The samples were drop-cast from a suspension in methanol, dried under a stream of nitrogen, and introduced into the UHV system *via* a loadlock under inert gas (N_2) flux, in order to minimize exposure to air contaminants, and kept in the introduction chamber for at least 12 hours before the measurements.

UV-Vis diffuse reflectance spectroscopy (DRS). The UV-Vis DRS spectra were measured on the solid samples with a Shimadzu UV-2600 spectrometer using an integrating sphere with $BaSO_4$ as a reference material. By using the Kubelka–Munk equation, Tauc plots were obtained, and the optical band-gap energy of the samples was extrapolated.

Raman spectroscopy. Raman spectroscopic characterization of the samples was performed at room temperature in a backscattering configuration using a LabRam HR 800EVO Raman spectrometer (Horiba France SAS) equipped with an Olympus BXFM microscope (objective X100, NA 0.9), TE cooled CCD detector (Syncerity OE), 633 nm HeNe laser, and a 600 grooves per mm diffraction grating. The spectral resolution was 0.9–1.8 cm^{-1}. The sample was drop-cast on silicon wafers as the substrate, then dried in a nitrogen atmosphere. The laser power at the sample was 0.7 mW, and the acquisition time was 1 s. Ten to twenty spectra were registered for each sample at different locations to verify sample homogeneity and the absence of photoinduced phenomena. The reference spectrum of Si was measured contextually in each sample. Raman spectra were corrected for the baseline, and peak analysis was performed using the Lorentzian fitting function to calculate the position, intensity and area of the characteristic peaks.

X-ray absorption spectroscopy (XAS). XAS data at the Co–K (7709 eV) and Ti–K (4966 eV) absorption edges were collected at the LISA beamline at the European Synchrotron Radiation Facility in Grenoble (France).[18] The monochromator was equipped with a pair of flat Si(111) crystals, whereas Si-coated mirrors (E_{cutoff} = 15 keV) were used for harmonic rejection. Spectra were collected under moderate vacuum (10^{-3} mbar) with cooling to around −190 °C with liquid nitrogen, in transmission mode, in the EH1 cabin of the beamline, where the beam is not focused.

Ion chambers filled with nitrogen gas at ambient pressure were used for data collection. Samples were prepared by mixing the powders with h-BN as a binder and pressing. After the sample was analyzed, the spectrum of a reference foil was collected for the same duration as the sample. In this way, a precise calibration of the energy scale was always ensured.

Raw XAS data were extracted with the ATHENA code[19] and quantitatively fitted with the ARTEMIS code.[19] Theoretical paths for the EXAFS analysis were calculated with the Feff84 code[20] starting from a 256-atom cluster derived from the CoP structure. The charge density was calculated in self-consistent form, and the correlation-exchange part of the potential was in the Hedin–Lundqvist approximation. Data were fitted in R space after transformation of the XAS data in the interval 3–13 $Å^{-1}$ with a k^2 weight.

Photocatalytic H_2 production

The photocatalytic hydrogen evolution experiments were performed in a 30 mL cylindrical quartz reactor at ambient temperature (T = 25 °C). 1.8 mg of catalyst was ultrasonically dispersed in 4 mL of degassed MilliQ water and 1 mL of methanol, and the quartz reactor was closed with a rubber cap equipped with a silicone septum. A 300 W Xe lamp (mKs-Newport) equipped with a band cut-off filter ($\lambda \leq 780$ nm) was used as the light source. Stirring was started when the sample was irradiated with light. The measurements were carried out while irradiating in the UV-Vis region at a light intensity of 1.4 sun (140 mW cm^{-2}), which was calibrated using a Si reference cell. Before irradiation, nitrogen gas was bubbled for 30 min to remove the air. The evolved hydrogen gas was sampled every hour and determined using an off-line gas chromatograph (Shimadzu GC-2010) equipped with a thermal conductivity detector (TCD) and a 5 Å molecular sieve column.

Electrochemical measurements

Electrochemical measurements, including electrochemical impedance spectra (EIS) and specific capacitance performances (cyclic voltammetry, CV), were carried out in a standard three-electrode cell on an electrochemical workstation (PARSTAT 2273 potentiostat). The EIS (perturbation voltage 20 mV, frequency 110 kHz–100 mHz) and CV were measured using an Ag/AgCl electrode as the reference electrode, a platinum plate as the counter electrode, and 0.5 M Na_2SO_4 aqueous solution as the electrolyte. To prepare the working electrode, pristine TiO_2, BP, and the nanocomposites BP@Co_xP and TiO_2/BP@Co_xP were dispersed in acetone having a final concentration of 2.0 mg mL^{-1}. The dispersion containing the catalyst was deposited by drop-coating on a fluorine-doped tin oxide (FTO) conductive glass substrate (2.0 cm^2) and was dried under a stream of nitrogen before measurements. Mott–Schottky (M–S) curves were measured under an arc amplitude of 10 mV and frequency of 1 kHz.

Photoluminescence (PL)

PL measurements were registered using a Jasco spectrofluorometer model FP-8300. The powder samples TiO_2 and TiO_2/BP@Co_xP were analyzed by irradiating at a wavelength close to the maximum absorption in the corresponding UV-Vis spectrum (λ = 325 nm).

Results and discussion

BP nanosheets (NS) were obtained *via* liquid-phase exfoliation of bulk BP under the action of ultrasound for a prolonged time,[9] and their functionalization with cobalt was achieved by a mild solvothermal procedure in which $Co(CH_3COO)_2$ was added to a BPNS suspension in dry DMF, and the mixture was heated at T = 180 °C for 4 h in an autoclave. Three different nanohybrid BP-Co were synthesized with 10, 20 and 30 wt% Co loading, respectively. Afterwards, the assembly with TiO_2 nanoparticles was performed *via* ultrasonication, driven by electrostatic interactions. TiO_2 has a positive Z potential of 14.1 ± 0.5 mV, whereas BP-Co has a negative zeta value (−14.7 mV, −12.4 mV and −10.9 mV for 10%, 20% and 30 wt% of Co, respectively), in agreement with pristine BP having a more negative Z-potential of −38.0 ± 0.5 mV. Thus, correspondingly, a series of different ternary TiO_2/BP-Co nanocomposites were obtained, and their extensive characterization by electron microscopy, XRD and Raman spectroscopy was carried out. Careful TEM imaging at different magnifications was performed on several BP-Co flakes, and, intriguingly, no cobalt nanoparticles were detected on their surface (Fig. 1a and b). However, elemental mapping revealed the presence of cobalt spread over the entire surface of the BP flake (Fig. 1c and d), which implies the presence of cobalt as either nanoclusters with a size less than 1 nm or even single atoms.

Selected area electron diffraction (SAED) was performed on $BP@Co_{20}$ to investigate the crystallographic structure of the system. The resulting electron diffraction pattern exhibited the crystallographic spots ascribable to orthorhombic CoP and Co_2P phases (space group *Pnma*, 62) (Fig. 2e).[21,22] The coexistence of these two phases can be induced by the different concentrations of the cobalt precursor on the BP surface, which, upon reaction and interaction with P atoms, led to the simultaneous formation of CoP and Co_2P. These compounds were named Co_xP and the nanohybrid as $BP@Co_xP$.

The ternary nanocomposite $TiO_2/BP@Co_xP$ was analysed by TEM, and the BP nanoflakes were found to be fully covered by TiO_2 NPs (average dimension 20 nm ± 2 nm). Moreover, from the elemental mapping analysis, cobalt was found to be evenly distributed on the flakes (Fig. S1).

Powder X-ray diffraction shows very narrow peaks for BP, due to its high crystallinity, at 2θ = 16.9°, 26.3°, 34.1°, 34.9°, 50.7°, 52.4°, 55.8°, 56.9°, which correspond to the planes[23] (020), (021), (040), (111), (112), (060), (151) and (132), respectively. These peaks are also observed in $BP@Co_xP$, albeit with varying intensity (Fig. 2a), indicating that, during functionalization with cobalt, both the crystallinity and the structural integrity of BP were preserved. No characteristic diffraction peaks of CoP/Co_2P were found in $BP@Co_xP$ or $TiO_2/BP@Co_xP$ (see Fig. S2), confirming the very small size of the cobalt species. Raman spectra also confirm that the successive functionalization of BP with cobalt and then with TiO_2 does

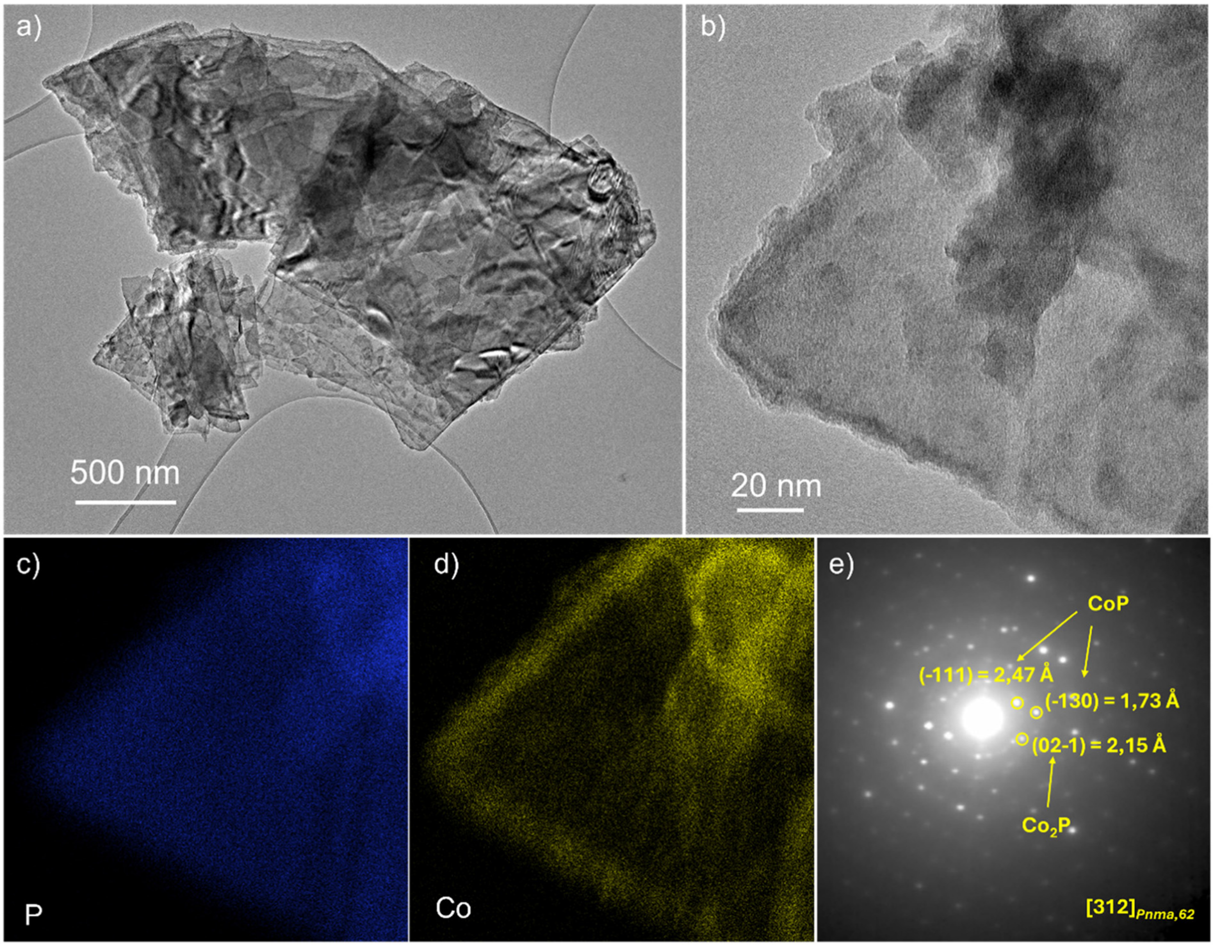

Fig. 1 (a and b) TEM of BP flakes functionalized with cobalt, named as $BP@Co_{20}$, at different magnifications. (c and d) Elemental mapping of the flake. (e) SAED pattern.

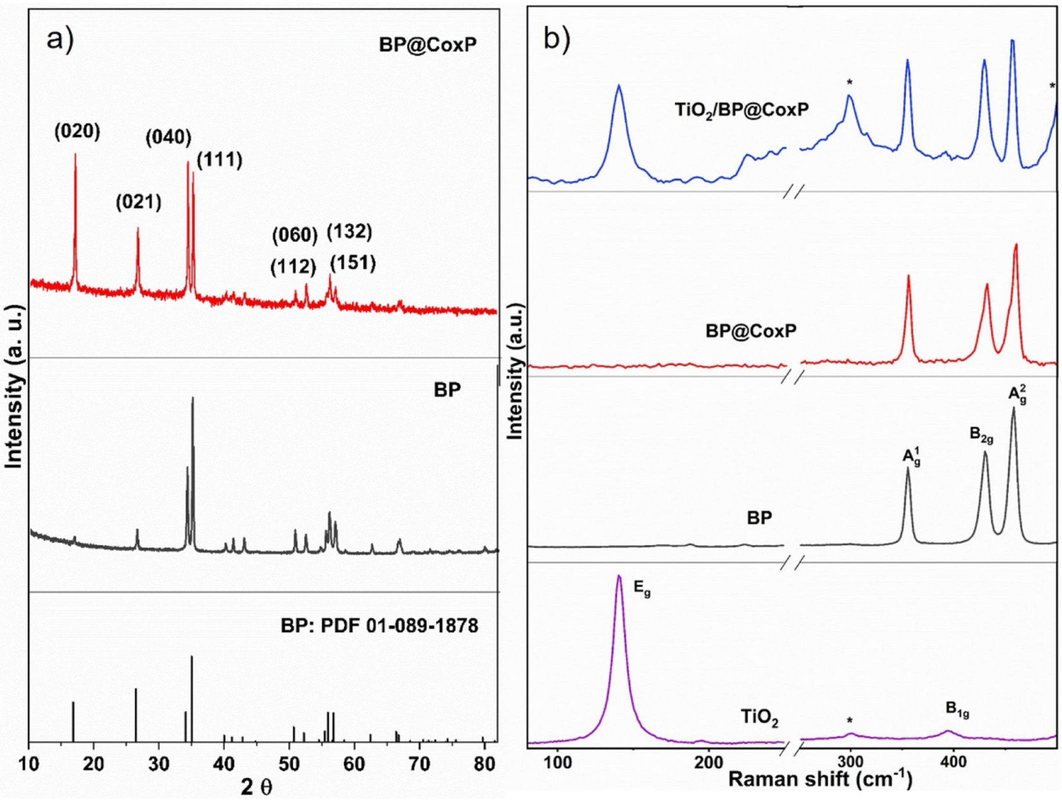

Fig. 2 (a) PXRD analysis of pristine BP, BP@Co_xP and of TiO_2/BP@Co_xP. (b) Comparison of the Raman spectra of TiO_2, BP, BP@Co_xP and TiO_2/BP@Co_xP.

not alter the typical pattern of BP. As shown in Fig. 2b, three Raman modes are observed at 360 cm^{-1}, 436 cm^{-1} and 464 cm^{-1}, corresponding to the out-of-plane $A^1{}_g$, in-plane B_{2g}, and the $A^2{}_g$ phonon mode of orthorhombic BP.[24] In the ternary TiO_2/BP@Co_xP, beyond the BP fingerprint, the characteristic Raman peaks of anatase TiO_2 were identified at 141 cm^{-1} and 394 cm^{-1}, which correspond to the E_g and B_{1g} phonon modes of O–Ti–O bond vibration, respectively.[25]

To unravel the chemical state of Co and P in the nanocomposite, XPS analysis was performed. The core-level Co 2p spectrum (Fig. 3a) of TiO_2/BP@Co_xP can be fitted with two main peaks at BE = 777.8 eV and 792.8 eV, separated by a spin–orbit split of 15.0 eV, which can be attributed to Co $2p_{3/2}$ and Co $2p_{1/2}$, respectively, of metallic cobalt $Co^{(0)}$ or cobalt phosphide $Co^{\delta+}$.[26] In addition, two peaks arising at BE = 781.6 eV and 797.0 eV are ascribed to CoO_x (Co^{3+}) species. The minor peaks at BE = 786.0 eV and 803.8 eV are attributed to CoO_x (Co^{2+}) species, which are quite commonly found as a superficial layer in cobalt-functionalized materials.[27,28] The core level P 2p spectrum of TiO_2/BP@Co_xP (Fig. 3b) shows two main peaks at BE = 128.9 eV and 129.7 eV assigned to P $2p_{3/2}$ and P $2p_{1/2}$, respectively, which are both shifted to lower BE with respect to pristine elemental BP, which has two characteristic peaks at BE = 129.5 eV and 130.4 eV, respectively, as shown in Fig. S3a. This reveals clearly the presence of negative valence P ($P^{\delta-}$) in the ternary composite, which can be safely attributed to its phosphide nature, in agreement with the Co 2p spectrum. The peak at higher binding energy, BE = 133.1 eV in Fig. 3b, can be deconvoluted into two peaks: one at BE = 133.5 eV, attributed to the formation of a layer of phosphorus oxide,[29] and the second at BE = 132.6 eV, which is in the region typical of metal-phosphorus interactions[30] and thus can be assigned to the Co–P bond. The Ti 2p spectrum shows two peaks at BE = 458.5 eV and 464.3 eV, see Fig. S3c, that correspond to Ti $2p_{3/2}$ and Ti $2p_{1/2}$, respectively, which are shifted to higher BE of +0.4 eV and +0.5 eV with respect to pristine TiO_2, having two peaks at BE = 458.1 eV and 463.8 eV (see Fig. S3b), indicating the presence of an interfacial interaction of TiO_2 with BP and Co.[8]

Aiming to gain insight into the overall structure of BP@Co_xP in the bulk, Co K-edge extended X-ray absorption fine structure (EXAFS) spectroscopy was used to study the coordination environments of cobalt. In Fig. 4a the EXAFS spectra of BP@Co_xP, TiO_2/BP@Co_xP and BP@Co_xP aged one year in ambient conditions are shown, while the corresponding Fourier transforms (FT) plots are collected in Fig. 4b. FT of BP@Co_xP shows a predominant peak at 1.7 Å and a minor peak at 2.6 Å (note that these values are not the real interatomic distances, as these FTs are not phase-corrected). By comparison with the Co metal foil and Co_3O_4 and on the basis of a quantitative fit (the results of which are shown in Table S1), the first peak can be attributed to a Co–P bond, whereas the second is assigned to a Co–Co correlation. Taking into account that the

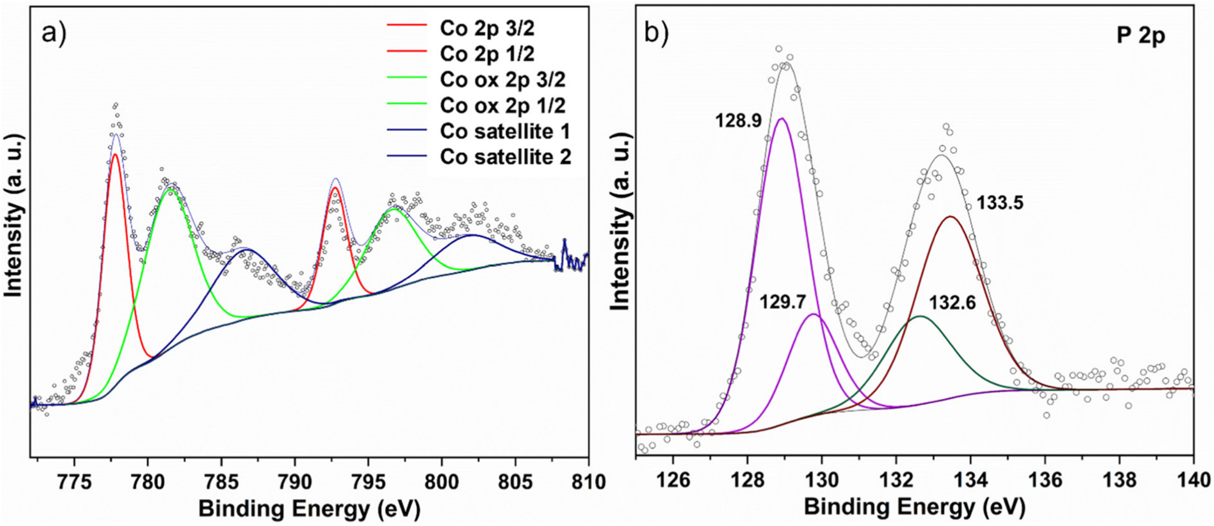

Fig. 3 Core level XPS spectra of (a) Co 2p and (b) P 2p of $TiO_2/BP@Co_xP$.

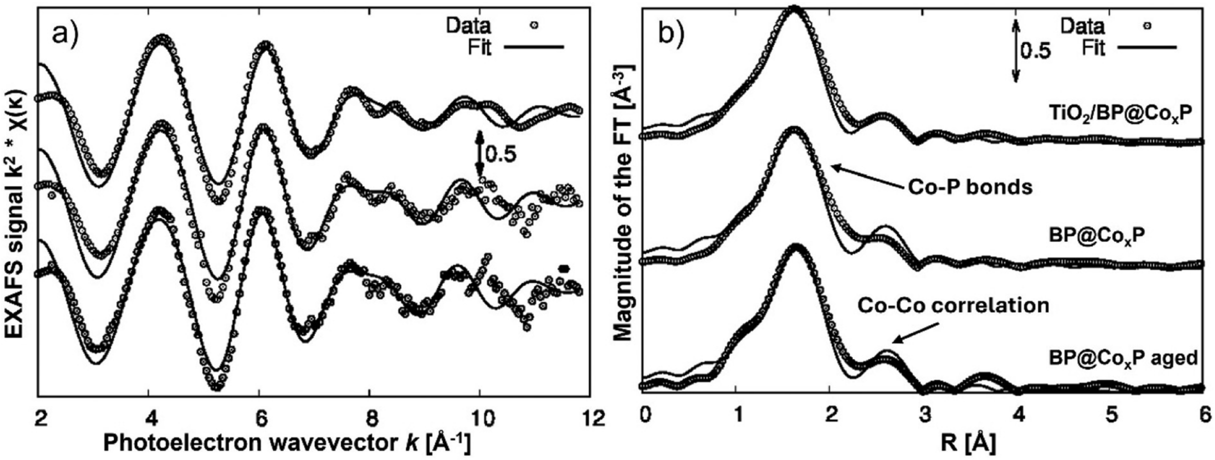

Fig. 4 (a) Co-EXAFS spectra of the samples $TiO_2/BP@Co_xP$, $BP@Co_xP$ and $BP@Co_xP$ aged (dots) with the best fit (lines). (b) Fourier transforms (FT) of the EXAFS spectra of the same samples; dots indicate experimental data, while continuous lines are calculated best-fit data.

coordination number of cobalt towards P is $N = 4$, and the Co–P distance $R_{Co-P} = 2.23$ Å, which is the same as found in Co(I) and Co(II) triphenylphosphine complexes used as standard and slightly less than that of bulk CoP, see Table S1, it is reasonable to infer that Co atoms are bonded to the P atoms of phosphorene. Given that Co–O bond distance is sensibly shorter, being $R_{Co-O} = 2.13$ Å in the model compound CoO where Co is 6-coordinated, we can rule out the presence of cobalt oxide in our sample. Furthermore, the minor peak in the FT can be fitted with a Co–Co shell at ≈3 Å. This value is considerably longer than that observed in metallic Co ($R_{Co-Co} = 2.5$ Å)[31] and shorter than that in Co_3O_4 ($R_{Co-Co} = 3.35$ Å),[32] allowing these phases to be ruled out. Thus, we can assume that $BP@Co_xP$ does not contain $Co^{(0)}$ NPs or cobalt oxide NPs. The ternary composite $TiO_2/BP@Co_xP$ showed exactly the same pattern as $BP@Co_xP$, indicating the integration with TiO_2 NPs does not alter the structure of $BP@Co_xP$.

Intriguingly, the sample of $BP@Co_xP$ kept under ambient conditions for one year showed the same EXAFS pattern, with a negligible peak due to a Co–O bond (see the shoulder at 1.2 Å in Fig. 4b for $BP@Co_xP$ aged), meaning that the surface functionalization with cobalt prevented the degradative oxidation of BP.[13] This can be explained by taking into account that the Fermi level of BP is known to be higher than that of Co or its derivatives, and electron migration is expected to occur from BP to Co or its derivatives.[33,34] In this way, the lone pairs of the P atoms of BP are no longer available for interaction with water or oxygen molecules, and the integrity of BP is preserved.

Measurements at the Ti-K edge were also performed for the TiO_2/BP and $TiO_2/BP@Co_xP$ samples and compared with those of standard TiO_2 anatase. The XANES data at the Ti-K edge shows that the spectra of TiO_2/BP and $TiO_2/BP@Co_xP$ are superimposable (see Fig. S4), thus the oxidation state of TiO_2 is not affected by the functionalization with BP or cobalt.

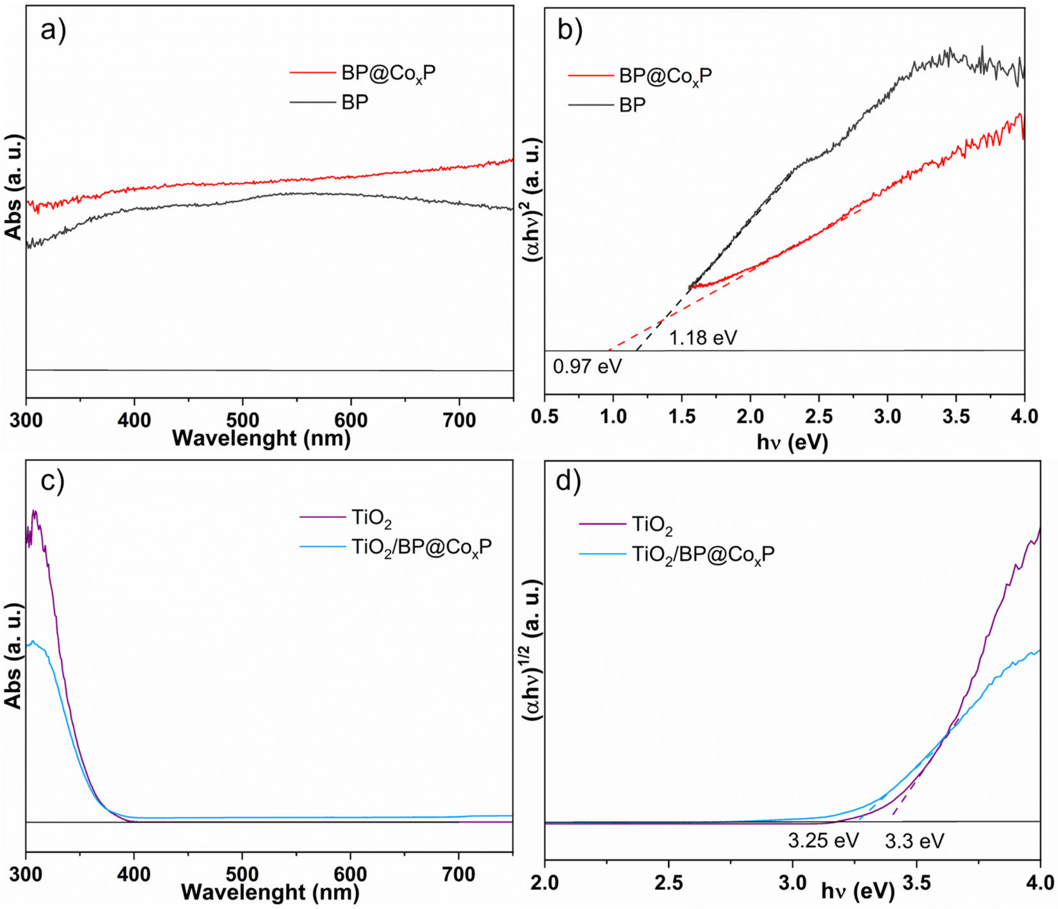

Fig. 5 UV-Vis spectra of (a) binary and (c) ternary nanocomposites. Tauc plots of (b) binary and (d) ternary composites.

EXAFS spectra at the Ti-K edge are shown in Fig. S5–S7. From the comparison of TiO_2/BP and TiO_2/BP@Co_xP with pristine TiO_2, it is evident that the binary and ternary composites share the same structural parameters with the parent TiO_2 (see Table S2). Thus, there are only weak interfacial interactions between TiO_2 and BP. This agrees well with a computational study[35] showing that the interaction in TiO_2/BP heterostructures occurs primarily through physisorption, and contrasts with previous studies that proposed the formation of covalent P–O–Ti bonds between TiO_2 and the BP surface.[36]

To evaluate the opto-electronic properties, UV-Vis DRS spectra were registered, and the resulting Tauc plot showed that passing from BP to the binary BP@Co_xP, there is a slight decrease of band gap, $\Delta = -0.21$ eV (Fig. 5a and b), as already observed with the functionalization of BP with Ni NPs.[14] The integration of BP@Co_xP with TiO_2 NPs caused a narrowing of the TiO_2 band gap, shifting the absorption of the composite towards the visible region (Fig. 5c and d).

Photocatalytic H_2 production

Firstly, screening of TiO_2/BPNS nanocomposites with variable amounts of BPNS in the range 1.0–4.0 wt% was carried out. The photocatalyst was dispersed in a water/methanol solution (4 : 1), with methanol selected as the hole scavenger, and irradiated in the UV-Vis region with a 300-Watt Xe lamp. It emerged that increasing the loading of BPNS on TiO_2 led to a drop in the catalytic activity from H_2 = 1.03 mmol h^{-1} g^{-1} (for BP = 1%) to H_2 = 0.3 mmol h^{-1} g^{-1} (for BP = 4%), as shown in Fig. S8. Considering this result, a screening of TiO_2-based nanocomposites with a BP content in the range 1.0%–3.0 wt%, and a fine tuning of Co wt% in the range 0.1–0.9%, was carried out.

To reach the goal, three different binary BP@Co_xP were prepared with increasing amounts of cobalt (10, 20 and 30 wt%), which were then loaded on TiO_2 by ultrasonication. As clearly shown in Fig. 6, at 1.0% BP, the HER rate is moderately low (1.9 mmol g^{-1} h^{-1}), but at higher amounts of BP (2.0% and 3.0%), the HER rate increases drastically. By fine-tuning the Co wt%, $TiO_2/BP_{2\%}@Co_xP_{0.8\%}$ was identified as the best performing catalyst, affording 5.3 mmol g^{-1} h^{-1} of H_2, which is 30 times and 9 times higher than for pristine TiO_2 (H_2 = 0.18 mmol h^{-1} g^{-1}) and $TiO_2/BP_{2\%}$ (H_2 = 0.57 mmol h^{-1} g^{-1}, see Fig. S8), respectively. This result highlights the pivotal role of Co_xP and that HER mainly takes place at the Co_2P/CoP site.

From a literature search summarized in Table S3, the figure of merit of this work lies on the limited amount of non noble metal used and the role of BP@Co_xP as co-catalyst that boosts

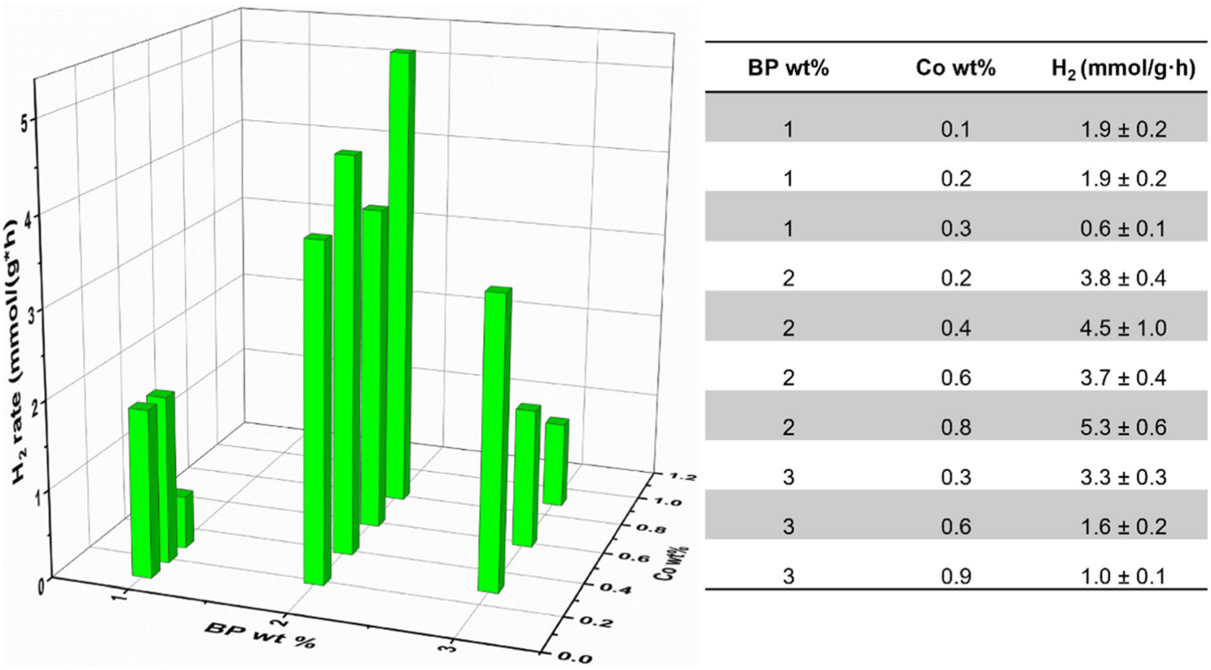

BP wt%	Co wt%	H_2 (mmol/g·h)
1	0.1	1.9 ± 0.2
1	0.2	1.9 ± 0.2
1	0.3	0.6 ± 0.1
2	0.2	3.8 ± 0.4
2	0.4	4.5 ± 1.0
2	0.6	3.7 ± 0.4
2	0.8	5.3 ± 0.6
3	0.3	3.3 ± 0.3
3	0.6	1.6 ± 0.2
3	0.9	1.0 ± 0.1

Fig. 6 Left side: comparison of the H_2 production rates using different amounts of BP and Co integrated in the TiO_2 nanostructures. Right side: a table of the catalytic data and corresponding errors in the measurements.

the rate respect with similar system as $TiO_2/CoPx_{0.5\%}$.[37] To assess the robustness of the photocatalyst, its stability to cycling was evaluated. Satisfyingly, after six runs, the amount of H_2 evolved was essentially constant, as shown in Fig. S9, demonstrating the high stability of the photocatalyst under irradiation. TEM analysis coupled with STEM EDS confirmed that the nanostructured catalyst is unaltered after recycling, as shown in Fig. S10.

Electrochemical properties and charge dynamics

The conduction band (CB) and valence band (VB) energy levels of the single semiconductors, BP and TiO_2, and of the nanocomposites BP@Co_xP and TiO_2/BP@Co_xP, were determined using Mott–Schottky measurements. As displayed in Fig. 7a, the Mott–Schottky plot gives a flat band potential, V_{FB}, from the intersection with the *x*-axis and, interestingly, once BP is functionalized with *in situ* grown cobalt, there is a reduction of both flat band potential V_{FB} from −0.43 to −0.27 V[38] and of the slope of the curve. Meanwhile, the ternary nanocomposite TiO_2/BP@Co_xP has a $V_{FB} = -0.92$ V with a dramatic reduction of the slope (−0.49 V). According to eqn (1), the density of the charge carrier (N_D) is inversely proportional to the linear slope (k) in the Mott–Schottky plots, indeed the carrier concentrations in BP@Co_xP ($N_D = 7.82 \times 10^{19}$) and TiO_2/BP@Co_xP ($N_D = 1.21 \times 10^{20}$) are higher than those of the bare BP ($N_D = 4.77 \times 10^{19}$) and TiO_2 ($N_D = 2.41 \times 10^{19}$), respectively.

$$N_D = \frac{2}{\varepsilon \cdot \varepsilon' \cdot e \cdot k} \tag{1}$$

The functionalization of BP with mixed phosphides Co_2P/CoP brings a noteworthy increase in the carriers' density and a strongly negative V_{FB}, which means a conduction band with much higher reducing power in comparison to the parent TiO_2 and BP, which well explains the improved rate of hydrogen evolution. Assuming that the conduction band is approximately 0.1 V more negative than V_{FB}, the calculated $E_{(CB\ vs.\ NHE)}$ for TiO_2, BP, BP@Co_xP and TiO_2/BP@Co_xP was found to be −0.22, −0.23, −0.17, and −0.82 V, respectively. The band gaps for TiO_2, BP and BP@Co_xP were 3.3 eV, 1.18 eV and 0.97 eV, respectively, as shown in Fig. 5; thus, the $E_{(VB\ vs.\ NHE)}$ were 3.08 V, 0.74 V, and 0.8 V, respectively. With these data, the band structure of BP@Co_xP and TiO_2, as illustrated in Fig. S11, shows a type I heterojunction.

Electrochemical impedance spectroscopy (EIS) measurements showed TiO_2/BP@Co_xP has by far the smallest arc radius in comparison to the parent TiO_2 and BP (Fig. 7b), indicating a dramatic increase in the charge-transfer rate arising from a strong interfacial interaction between the n-type TiO_2 and p-type BP@Co_xP that creates an internal electric field. To quantify the charge-transport properties, Nyquist plots were fitted with an equivalent circuit (Fig. 7b inset), and the charge-transfer resistance (R_1, R_2) and the pseudocapacitance Q_2 were determined (see Table S4).

Pristine BP showed the highest R_1 and R_2 values (139.9 Ω and 76 634 Ω, respectively); meanwhile, the ternary TiO_2/BP@Co_xP has the least resistance to charge transfer ($R_1 = 25.61$ Ω, $R_2 = 4200$ Ω).

Steady-state photoluminescence was measured (see Fig. S12), and going from pure TiO_2 to the composites TiO_2/BP@Co_xP, a quenching of the emission was observed, meaning a diminution of electron–hole recombination, which

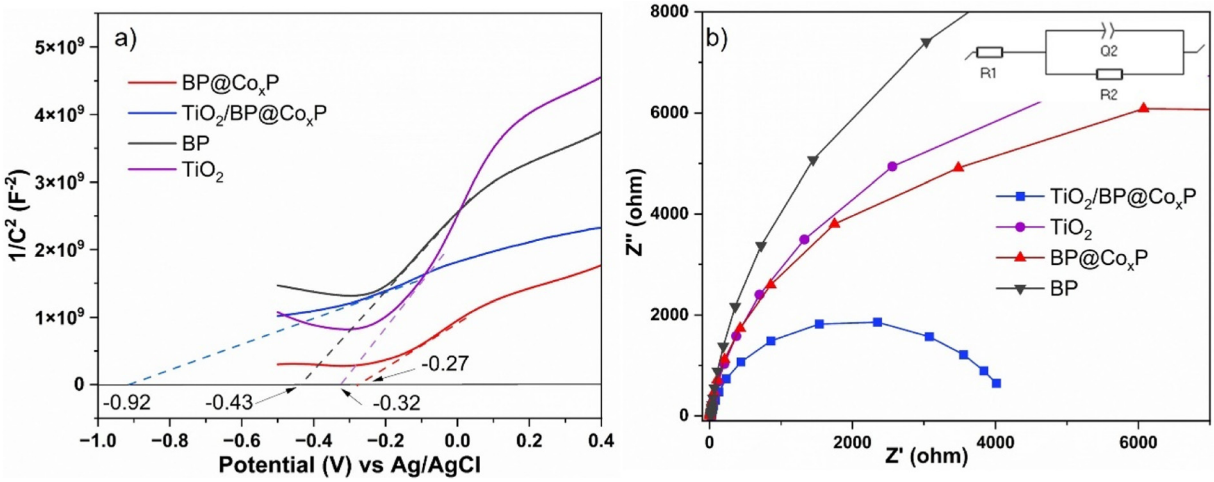

Fig. 7 (a) Mott–Schottky plots of TiO_2 and BP and the nanocomposites $BP@Co_xP$ and $TiO_2/BP@Co_xP$. Dashed lines show an approximate linear fit used to estimate the V_{FB}. (b) Nyquist plot of TiO_2, BP, $BP@Co_xP$ and $TiO_2/BP@Co_xP$ measured in a 0.5 M Na_2SO_4 solution with an inset of the equivalent circuit. The symbols correspond to the measured data, and the lines represent the fitting results.

testifies to the establishment of a p–n junction between $BP@Co_xP$ and TiO_2, respectively, that efficiently contributes to the charge separation.

Conclusions

Using a one-step protocol that goes through cobalt functionalization of BPNS by a solvothermal reaction and induces the formation of a mixed phase CoP/Co_2P, we developed a highly active catalytic system at low Co content (<1.0 wt%), characterized by cobalt phosphide clusters with a size less than 1.0 nm, homogeneously dispersed on the surface of BP nanosheets. The structural and morphological information on the material was derived from both electron microscopy diffraction and EXAFS, and revealed the presence of Co–P bonds with lengths that fall in the range of cobalt phosphide and dative Co–P bonds in coordination complexes. Meanwhile, the absence of any direct Co–Co bond confirmed the absence of Co NPs. The XPS data are consistent with the presence of cobalt in a low oxidation state and phosphorus in both phosphide and elemental states. Additionally, EXAFS proved that the structural integrity of $BP@Co_xP$ was preserved after storing the material for one year under ambient conditions. Thus, given the stability and robustness of $BP@Co_xP$, we envisaged that the latter could be applied as a co-catalyst and integrated with TiO_2 NPs for solar-driven hydrogen production. Satisfyingly, the novel Co_xP clusters were effective in catalysing the HER with an increase in the reaction rate of 30 times, with respect to pure TiO_2; furthermore, the tested catalytic platform remained unaltered after six cycles. Electrochemical characterization evidences that the phosphide phases grown on BPNS bring a strong enhancement of charge-carrier density and dramatically lower the flat band potential ($\Delta = -0.6$ V) in $TiO_2/BP@Co_xP$ with respect to pristine TiO_2, inducing a much greater reduction power. Overall, these electronic properties make the system very appealing for further applications in the solar field.

Conflicts of interest

There are no conflicts to declare.

Data availability

All data needed to support the conclusions in the paper are presented in the paper and the supplementary information (SI). Supplementary information: HAADF-STEM images and EDS analysis, X-ray powder diffraction spectra, XPS spectra, EXAFS data, band energy level diagram, stability tests of catalytic activity, PL data, and catalytic tests with TiO_2/BP. See DOI: https://doi.org/10.1039/d6nr00321d.

Acknowledgements

This work has been funded by the European Union-NextGenerationEU, Mission 4, Component 1, under the Italian Ministry of University and Research (MUR) National Innovation Ecosystem grant ECS00000041-VITALITY-CUP B43C22000470005. XAS experiments were performed at the LISA-BM08 beamline (ESRF, Grenoble, France) through the CERIC-ERIC user access. To the experiment, it was assigned the CERIC code 20242170 and ESRF code A08-1-1125 and the data have the https://doi.org/10.15151/ESRF-ES-1915447087. LISA is financed by the Consiglio Nazionale delle Ricerche, project DFM.AD006.072.

References

1 S. B. Beil, S. Bonnet, C. Casadevall, R. J. Detz, F. Eisenreich, S. D. Glover, C. Kerzig, L. Næsborg, S. Pullen, G. Storch, N. Wei and C. Zeymer, *JACS Au*, 2024, **4**, 2746–2766.

2 X. Leng, K. Yang, L. Sun, J. Weng and J. Xu, *Angew. Chem., Int. Ed.*, 2025, **64**, e202416992.

3 M. Zhao, R. Zhang, Z. Fu, H. Xiao, M. Bai, L. Zhang, J. Zhang, J. Jia and N. Yang, *Int. J. Hydrogen Energy*, 2024, **53**, 263–272.

4 G.-Q. Zhao, J. Hu, X. Long, J. Zou, J.-G. Yu and F.-P. Jiao, *Small*, 2021, **17**, 2102155.

5 S. Moradian, A. Badiei, G. M. Ziarani, F. Mohajer, R. S. Varma and S. Iravani, *Environ. Res.*, 2023, **237**, 116910.

6 H. Tian, H. Wang, J. Wang, G. Qu, X.-F. Yu and G. Jiang, *Acc. Mater. Res.*, 2024, **5**, 1472–1483.

7 W. Gao, Y. Zhou, X. Wu, Q. Shen, J. Ye and Z. Zou, *Adv. Funct. Mater.*, 2021, **31**, 2005197.

8 A. Ozawa, M. Yamamoto, T. Tanabe, S. Hosokawa and T. Yoshida, *J. Mater. Chem. A*, 2020, **8**, 7368–7376.

9 X. Ren, L. Shi, Y. Li, S. Song, Q. Wang, S. Luo, L. Ren, H. Zhang, Y. Izumi, X. Peng, D. Philo, F. Ichihara and J. Ye, *ChemCatChem*, 2020, **12**, 3870–3879.

10 E. J. Popczun, C. G. Read, C. W. Roske, N. S. Lewis and R. E. Schaak, *Angew. Chem., Int. Ed.*, 2014, **53**, 5427–5430.

11 Q. Wang, L. Kong, J. Xu, B. Zhou, X. Liu, Z. Lin, S. Shi, X. Zhang and L. Li, *ACS Sustainable Chem. Eng.*, 2024, **12**, 11717–11727.

12 Q. Liang, F. Shi, X. Xiao, X. Wu, K. Huang and S. Feng, *ChemCatChem*, 2018, **10**, 2179–2183.

13 Y.-J. Yuan, Z.-K. Shen, S. Song, J. Guan, L. Bao, L. Pei, Y. Su, S. Wu, W. Bai, Z.-T. Yu, Z. Ji and Z. Zou, *ACS Catal.*, 2019, **9**, 7801–7807.

14 G. Provinciali, J. Filippi, A. Lavacchi, S. Caporali, M. Banchelli, M. Serrano-Ruiz, M. Peruzzini and M. Caporali, *ChemCatChem*, 2023, **15**, e202300647.

15 M. Köpf, N. Eckstein, D. Pfister, C. Grotz, I. Krüger, M. Greiwe, T. Hansen, H. Kohlmann and T. Nilges, *J. Cryst. Growth*, 2014, **405**, 6–10.

16 M. Serrano-Ruiz, M. Caporali, A. Ienco, V. Piazza, S. Heun and M. Peruzzini, *Adv. Mater. Interfaces*, 2016, **3**, 1500441.

17 Y. Xu, W. Zhang, G. Zhou, M. Jin and X. Li, *J. Colloid Interface Sci.*, 2022, **616**, 641–648.

18 F. d'Acapito, G. O. Lepore, A. Puri, A. Laloni, F. La Manna, E. Dettona, A. De Luisa and A. Martin, *J. Synchrotron Radiat.*, 2019, **26**, 551–558.

19 B. Ravel and M. Newville, *J. Synchrotron Radiat.*, 2005, **12**, 537–541.

20 A. L. Ankudinov, B. Ravel, J. J. Rehr and S. D. Conradson, *Phys. Rev. B: Condens. Matter Mater. Phys.*, 1998, **58**, 7565–7576.

21 K. Selte, L. Birkeland and A. Kjekshus, *Acta Chem. Scand., Ser. A*, 1978, **32**, 731–735.

22 H. N. Nowotny, *Z. Anorg. Allg. Chem.*, 1947, **254**, 31–36.

23 Y. Kim, I. K. Park, D. C. Yang, D. Y. Kim, G. Lee and N. Kim, *Phys. Rev. B*, 2025, **111**, L161407.

24 D. Hanlon, C. Backes, E. Doherty, C. S. Cucinotta, N. C. Berner, C. Boland, K. Lee, A. Harvey, P. Lynch, Z. Gholamvand, S. Zhang, K. Wang, G. Moynihan, A. Pokle, Q. M. Ramasse, N. McEvoy, W. J. Blau, J. Wang, G. Abellan, F. Hauke, A. Hirsch, S. Sanvito, D. D. O'Regan, G. S. Duesberg, V. Nicolosi and J. N. Coleman, *Nat. Commun.*, 2015, **6**, 8563.

25 S. A. Bhandarkar, Prathvi, A. Kompa, M. S. Murari, D. Kekuda and R. K. Mohan, *Opt. Mater.*, 2021, **118**, 111254.

26 J. Wang, D. Liu, H. Huang, N. Yang, B. Yu, M. Wen, X. Wang, P. K. Chu and X.-F. Yu, *Angew. Chem., Int. Ed.*, 2018, **57**, 2600–2604.

27 H. Chen, L. J. Falling, H. Kersell, G. Yan, X. Zhao, J. Oliver-Meseguer, M. Jaugstetter, S. Nemsak, A. Hunt, I. Waluyo, H. Ogasawara, A. T. Bell, P. Sautet and M. Salmeron, *Nat. Commun.*, 2023, **14**, 6889.

28 A. Jena, T. R. Penki, N. Munichandraiah and S. A. Shivashankar, *J. Electroanal. Chem.*, 2016, **761**, 21–27.

29 M. Caporali, M. Serrano-Ruiz, F. Telesio, S. Heun, A. Verdini, A. Cossaro, M. Dalmiglio, A. Goldoni and M. Peruzzini, *Nanotechnology*, 2020, **31**, 275708.

30 M. Vanni, M. Bellini, S. Borsacchi, L. Calucci, M. Caporali, S. Caporali, F. d'Acapito, M. Geppi, A. Giaccherini, A. Ienco, G. Manca, A. M. Mio, G. Nicotra, W. Oberhauser, M. Serrano-Ruiz, M. Banchelli, F. Vizza and M. Peruzzini, *J. Am. Chem. Soc.*, 2021, **143**, 10088–10098.

31 B. Cordero, V. Gómez, A. E. Platero-Prats, M. Revés, J. Echeverría, E. Cremades, F. Barragán and S. Alvarez, *Dalton Trans.*, 2008, 2832–2838.

32 W. L. Smith and A. D. Hobson, *Acta Crystallogr., Sect. B*, 1973, **29**, 362–363.

33 F. Shi, Z. Geng, K. Huang, Q. Liang, Y. Zhang, Y. Sun, J. Cao and S. Feng, *Adv. Sci.*, 2018, **5**, 1800575.

34 F. Shi, K. Huang, Y. Wang, W. Zhang, L. Li, X. Wang and S. Feng, *ACS Appl. Mater. Interfaces*, 2019, **11**, 17459–17466.

35 G. Provinciali, M. Serrano-Ruiz, J. Filippi, B. Muzzi, M. Banchelli, S. Caporali, M. Peruzzini, G. Barcaro, S. Monti and M. Caporali, *Int. J. Hydrogen Energy*, 2025, **186**, 152071.

36 H. U. Lee, S. C. Lee, J. Won, B.-C. Son, S. Choi, Y. Kim, S. Y. Park, H.-S. Kim, Y.-C. Lee and J. Lee, *Sci. Rep.*, 2015, **5**, 8691.

37 R. Liang, Y. Wang, C. Qin, X. Chen, Z. Ye and L. Zhu, *Langmuir*, 2021, **37**, 3321–3330.

38 M. Vanni, M. Serrano-Ruiz, J. Filippi, M. C. Salvatici, E. Fonda, M. Peruzzini and M. Caporali, *ChemPlusChem*, 2023, **88**, e202200457.